

RESEARCH ARTICLE

Characteristics of cyclones following different pathways in the Gulf Stream region

Leonidas Tsopouridis^{ORCID} | Clemens Spensberger^{ORCID} | Thomas Spengler^{ORCID}

Geophysical Institute, University of Bergen, and Bjerknes Centre for Climate Research, Bergen, Norway

Correspondence

L. Tsopouridis, Geophysical Institute, University of Bergen, Postboks 7803, 5020 Bergen, Norway.

Email: leonidas.tsopouridis@uib.no

Funding information

Research Council of Norway (RCN), Grant/Award Number: 262220

Abstract

The Northwest Atlantic is a region of strong temperature gradients and hence is a favourable location for wintertime cyclone intensification co-located with the storm track. The temperature gradient is associated with both the sea surface temperature front along the Gulf Stream and the land–sea contrast. To understand the respective influences of the sea surface temperature (SST) front and land–sea contrast in the Gulf Stream region, as well as the role of upper-level forcing on cyclone development, we track individual cyclones and categorise them depending on their propagation relative to the SST front. We concentrate on cyclones staying either on the cold (C1) or warm (C2) side of the SST front, and on cyclones that cross the SST front from the warm to the cold side (C3). Comparing these categories, we find that the land–sea contrast is more important for supplying baroclinicity to cyclones in C1, while the strong low-level baroclinicity in C3 is also partially attributable to the SST front. The propagation of cyclones in C1 and C3 near the left exit region of the North Atlantic jet explains the higher intensification and precipitation.

KEYWORDS

cyclone intensification, Gulf Stream, extratropical cyclones, land–sea contrast, SST front

1 | INTRODUCTION

The western North Atlantic region is characterized by both strong sea surface temperature (SST) gradients associated with the Gulf Stream (Tomczak and Godfrey, 2003) and strong land–sea temperature contrasts during winter (Thompson *et al.*, 1988). The region is a preferential location for cyclogenesis (Hoskins and Hodges, 2002), cyclone intensification (e.g., Wang and Rogers, 2001; Lim and Simmonds, 2002; Jacobs *et al.*, 2008), and cyclonic bomb

formation (Sanders and Gyakum, 1980). Roebber (1989) indicated that the deepening rates of extratropical cyclones (hereafter cyclones) “arise as a sum of processes”, such as latent heat release (e.g., Rogers and Bosart, 1991; Kuo *et al.*, 1991; Whitaker and Davis, 1994) and baroclinic instability (e.g., Sanders, 1986; Manobianco, 1988; 1989; Catto, 2016). The origin of the baroclinicity has been argued to be due to the Gulf Stream SST gradient (Sanders, 1986) and the land–sea contrast (Wang and Rogers, 2001). We aim to clarify the relative roles of the SST front and the

land–sea contrast by categorising the intensification of cyclones in the Gulf Stream region with respect to their position relative to the SST front.

Several studies have highlighted the importance of diabatic heating and surface heat fluxes on maintaining low-level baroclinicity in the area of strong SST gradients (Kuo *et al.*, 1991; Reed *et al.*, 1993; Nakamura *et al.*, 2004; Hotta and Nakamura, 2011; Papritz and Spengler, 2015). Hotta and Nakamura (2011) underlined the significance of sensible heat fluxes for restoring low-level baroclinicity along oceanic frontal zones, while Papritz and Spengler (2015) emphasised latent heat release as a major contributor maintaining baroclinicity in the Gulf Stream region. The SST front has also been argued to increase convection and large-scale precipitation along the SST front (Minobe *et al.*, 2008; Parfitt *et al.*, 2016; Vanni re *et al.*, 2017b). However, studies based on composite analysis found cyclone intensity and moisture availability to be the dominant factors altering precipitation (Field and Wood, 2007; Rudeva and Gulev, 2011; Pfahl and Sprenger, 2016). Consistently, de Vries *et al.* (2019) found that cyclones respond to both the low-level baroclinicity associated with the SST front as well as the additional moisture provided by altered surface latent heat fluxes associated with changes in the SSTs.

In addition to the SST front, the wintertime temperature contrast between the cold continent to the west and the warmer ocean to the east can also influence the baroclinicity and the storm track (Cione *et al.*, 1993; Inatsu *et al.*, 2000; 2003; Brayshaw *et al.*, 2009; Booth *et al.*, 2012). In particular, Wang and Rogers (2001) and Brayshaw *et al.* (2009) showed that cyclones in the Northwest Atlantic are associated with a greater amount of baroclinicity due to their proximity to the land–sea boundary than cyclones in the Northeast Atlantic. Furthermore, the triangular shape of the North American continent together with the Rocky Mountains support the growth of the pool of cold air in the northeast of the continent, contributing to the surface temperature contrast along the Eastern North American continental margin which increases low-level baroclinicity and thereby cyclone intensification (Brayshaw *et al.*, 2009).

In addition to the low-level baroclinicity, the upper-level forcing, determined by the relative position of the jet stream, can contribute to cyclogenesis (e.g., Sanders and Gyakum, 1980; Uccellini *et al.*, 1984; Sinclair and Revell, 2000), as well as influence the subsequent evolution and intensification of cyclones (e.g., Evans *et al.*, 1994; Schultz *et al.*, 1998). Sanders and Gyakum (1980) noted that explosive cyclogenesis mainly occurs on the poleward side of the jet stream and is associated with an upper-level trough. This rapid cyclone intensification is due to the location close to the poleward exit region of the jet, because the upper-level divergence and vertical lifting stimulate both cyclone deepening and precipitation (e.g.,

Johnson and Daniels, 1954; Uccellini, 1990; Ritchie and Elsberry, 2003; Oruba *et al.*, 2013; Milrad, 2017).

To better understand the relative roles of the SST front, the land–sea contrast and upper-level forcing to cyclone intensification in the Gulf Stream region, we need to consider the evolution on synoptic time-scales (e.g., Parfitt *et al.*, 2016; Vanni re *et al.*, 2017b; Ogawa and Spengler, 2019). This can be accomplished either through composite analysis or by investigating individual case-studies. While case-studies can provide great detail of the different physical processes during the development of an individual cyclone, it is often difficult to draw more general conclusions on the dominant mechanisms. Analyses of composites of developing cyclones, on the other hand, have proven to be advantageous, as the basic features and general characteristics of the evolution are maintained, while not relying on arguments built around individual events with large case-to-case variability (Sinclair and Revell, 2000; Rudeva and Gulev, 2011).

For instance, using cyclone-centric composites, Wang and Rogers (2001) compared the dynamical structure and evolution of cyclones in different sectors of the North Atlantic. However, their analysis is based on explosive cyclones only. More recent studies evaluated surface heat fluxes and atmospheric moisture content for cyclones at different stages of their development over the Gulf Stream region (Rudeva and Gulev, 2011; Dacre *et al.*, 2020). However, none of these studies examined the specific contribution of the SST front to the intensification of cyclones. We thus complement these studies by including both explosive and non-explosive cyclones in the composite analysis and by evaluating the significance of the SST front on cyclone growth, where we divide cyclone propagation into different categories based on the path of cyclone trajectories relative to the SST front. Thereby, we shed light on the aspects of cyclone intensification in the Gulf Stream region and highlight the structural differences of cyclones following different paths relative to the Gulf Stream SST front.

2 | DATA AND METHODS

2.1 | Data

We use 6-hourly data from the ERA-Interim reanalysis (Dee *et al.*, 2011) with a horizontal resolution of $0.5^\circ \times 0.5^\circ$ for all winter months (December–February) in the period 1979–2016. Both cyclone intensity and distribution (Hodges *et al.*, 2011) as well as precipitation (Hawcroft *et al.*, 2012; Booth *et al.*, 2018) in ERA-Interim compare well to other reanalyses. For our analysis, we use mean sea level pressure (MSLP), SST, temperature at 850 hPa,

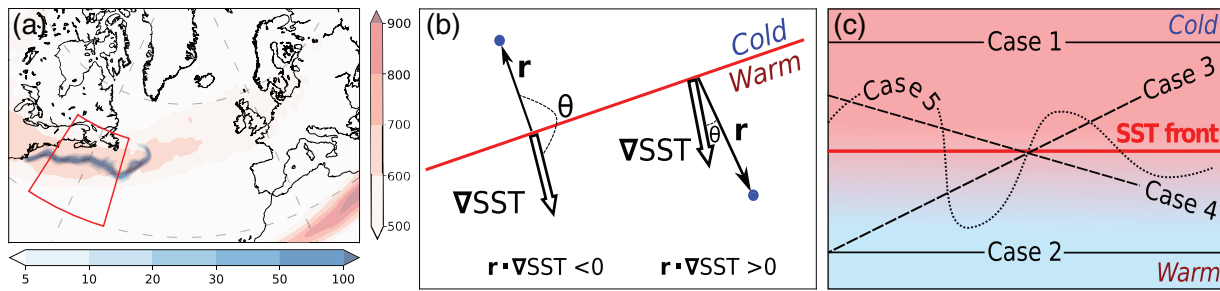


FIGURE 1 (a) Density of SST fronts ($\text{km of line (100 km)}^{-2}$, blue shading) and of the climatological jet stream ($\text{km of jet axis line (1000 km)}^{-2}$, light red shading) for the North Atlantic. The Gulf Stream region is marked with a red box. (b) Illustration describing the scalar product method to derive the relative position between the cyclone and the SST front. (c) Schematic of the cyclone classification based on the cyclone position relative to the SST front

total column water vapour (TCWV), vertically integrated water vapour flux (IWVF), wind at 925 hPa, large-scale and convective precipitation, as well as latent and sensible surface heat fluxes. Surface heat fluxes and precipitation are derived from the twice-daily forecasts (initialised at 0000 and 1200 UTC) and are accumulated ± 3 hr around the respective timesteps, following the same procedure as Ogawa and Spengler (2019) and Weijenborg and Spengler (2020). Specifically, we use the cumulative values from the 0000 UTC forecasts between 3 and 9 hr lead time, as well as between 9 and 15 hr lead time to derive fluxes and precipitation for the analyses of 0600 and 1200 UTC, respectively. Analogously, we use the 1200 UTC forecasts to derive precipitation and fluxes at 1800 and 0000 UTC.

2.2 | SST front detection

We identify SST fronts using an objective frontal detection scheme that is based on the “thermal” method (Hewson, 1998). This scheme has been applied to detect atmospheric fronts in several previous studies (Jenkner *et al.*, 2010; Berry *et al.*, 2011; Schemm *et al.*, 2015). The method by Hewson (1998) identifies frontal lines in a two-dimensional thermal field τ using the thermal frontal parameter (Renard and Clarke, 1965)

$$TFP = -\nabla|\nabla\tau| \cdot \frac{\nabla\tau}{|\nabla\tau|}, \quad (1)$$

where we chose τ to be the SST. The TFP indicates “the gradient of the magnitude of the gradient of a thermodynamic scalar quantity, resolved into the direction of the gradient of that quantity” (Renard and Clarke, 1965). Hewson (1998)’s framework is based on identifying the maxima of TFP, which correspond to the warm side of a frontal zone. In our study, however, we choose $TFP=0$ to identify the centre of the frontal zone (following e.g., Jenkner *et al.*,

2010), and apply a masking criterion

$$\nabla|\nabla\tau| < 0 \quad (2)$$

to exclude the detection of minima in SST gradients.

We perform the detection using SST data filtered with a triangular truncation T84 and require a minimum frontal length of 500 km to retain only fronts with a length-scale comparable to atmospheric fronts. To capture the most prominent parts of the SST fronts along the Gulf Stream, we found a temperature gradient threshold $|\nabla\tau| > 2\text{K}/100\text{ km}$ to yield the most accurate results. Consistent with oceanographic studies (e.g., Lee and Cornillon, 1996; Meinen and Luther, 2016), the SST front climatology for the North Atlantic basin features the highest frequency of SST fronts along the Gulf Stream (Figure 1a). To account for the convergence of the grid towards the poles, we normalise the front line detections to an average line length per unit area γ , with

$$\gamma = \frac{1}{AN} \sum_{i=1}^N l_i. \quad (3)$$

Here, A is the area covered by a grid cell, N the number of time steps in the climatology, and l_i the length of a SST front line over the respective grid cell during time step i (zero if no front is detected).

2.3 | Jet stream detection

To diagnose the role of upper-level forcing on cyclone intensification, we employ a jet detection, based on automatically detected jet axes, following the method and criteria of Spensberger *et al.* (2017). The jet axes are identified by lines separating the cyclonic from the anticyclonic wind shear. The climatological position of the North Atlantic jet

coincides with the location of the SST front (compare blue and light red shadings in Figure 1a).

2.4 | Cyclone detection and tracking

We employ the University of Melbourne cyclone detection and tracking algorithm (Murray and Simmonds, 1991a; 1991b). The algorithm defines cyclones as maxima in the Laplacian of the MSLP field and tracks them over time using a nearest-neighbourhood method together with the most probable direction of propagation (Murray and Simmonds, 1991a; 1991b; Michel *et al.*, 2018) The Appendix gives the chosen parameters.

For the selection of tracks, we require cyclones to spend at least 12 hr (three consecutive time steps) in the area of interest (30–50°N and 290–310°E), henceforth referred to as the Gulf Stream region. We also require that the minimum of pressure along the track occurs during December–February (DJF) and only consider tracks with maximum intensification, defined as the most rapid decrease in surface pressure, in the Gulf Stream region. In addition, we require the Great Circle distance between cyclogenesis and cyclolysis to be greater than 300 km to remove quasi-stationary systems. Furthermore, all cyclones positioned over terrain higher than 1000 m are discarded. By applying the criteria described above, we obtain 222 tracks over the 38 winters.

2.5 | Classification of cyclone tracks based on position to SST front

We find the shortest distance between each cyclone position and the SST front for every timestep along the cyclone track and define the vector \mathbf{r} directed from the SST front to the cyclone. We then use the scalar product

$$\mathbf{r} \cdot \nabla SST = |\mathbf{r}| |\nabla SST| \cos \theta \quad (4)$$

to calculate the angle θ between \mathbf{r} and ∇SST to detect which side of the SST front the cyclone is located (Figure 1b). If a cyclone is located on the warm (cold) side of the SST front, the scalar product is positive (negative). Note that the SST front lines do not have to follow the SST contours and that the front lines therefore do not have to be perpendicular to the SST gradient.

Using the relative position of the cyclone to the SST front within the Gulf Stream region, we categorise cyclone propagation into five categories (Figure 1c). For category 1 (C1) the cyclone always stays on the cold side of the SST front, while the cyclone always stays on the warm side of the SST front for category 2 (C2). Cyclones crossing the

SST front from the warm to the cold side belong to category 3 (C3), whereas they belong to category 4 (C4) if they cross the SST front from the cold to the warm side. Finally, cyclones that cross the SST front multiple times belong to category 5 (C5).

3 | RESULTS

3.1 | Cyclone occurrence and intensification

The cyclone density for the winter season (DJF) over the North Atlantic exhibits three major regions of cyclone activity: East of Greenland, the Gulf Stream, and along the Scandinavian coastline (Figure 2a). The cyclone density pattern is in good spatial agreement with previous studies (e.g., Hanley and Caballero, 2012; Neu *et al.*, 2013). We observe small quantitative differences compared to the density climatology presented by either Neu *et al.* (2013) or Murray and Simmonds (1991a), who also used the Melbourne University algorithm. These small deviations are most likely due to the neglect of shallow and weak systems in our database.

A large number of cyclones (84) stay on the cold side of the SST front (C1) (Figure 2b), whereas fewer cyclones (26) stay on the warm side of the SST front (C2) (Figure 2c). When crossing the SST front in the Gulf Stream region, the great majority of cyclones (64) cross the SST front towards its cold side (C3) (Figure 2d). A common feature for the three categories of cyclones is their propagation from the southwest to the northeast, whether or not they cross the SST front. Brayshaw *et al.* (2009) associated this tilt of the storm track with both the orientation of the North American east coast, as well as stationary waves from the Rocky Mountains. Only 13 cyclones cross the SST front from the cold to the warm side (C4) (Figure 2e) while 35 cyclones cross the SST front multiple times (C5) (Figure 2f). In order to assess the influence of the SST front on cyclones, we discard C4 and C5, because of the small number of tracks and multiple crossings, respectively. We will thus focus exclusively on C1, C2, and C3.

Cyclones in C1 and C2 never cross the SST front in the Gulf Stream region and mostly stay at a distance greater than 300 km on the cold or warm side, respectively (Figure 3a). In contrast, cyclones in C3 cross the SST front on average 6 hr after their maximum intensification (Figure 3a,b). Overall, cyclones in C1 and C3 feature the highest deepening rates (Figure 3b), with a maximum deepening rate of approximately $1.2 \text{ hPa} \cdot \text{h}^{-1}$ ($28 \text{ hPa} \cdot \text{day}^{-1}$), while cyclones of C2 experience a lower, yet notable intensification of $0.8 \text{ hPa} \cdot \text{hr}^{-1}$ ($19 \text{ hPa} \cdot \text{day}^{-1}$). C2 has a qualitatively similar,

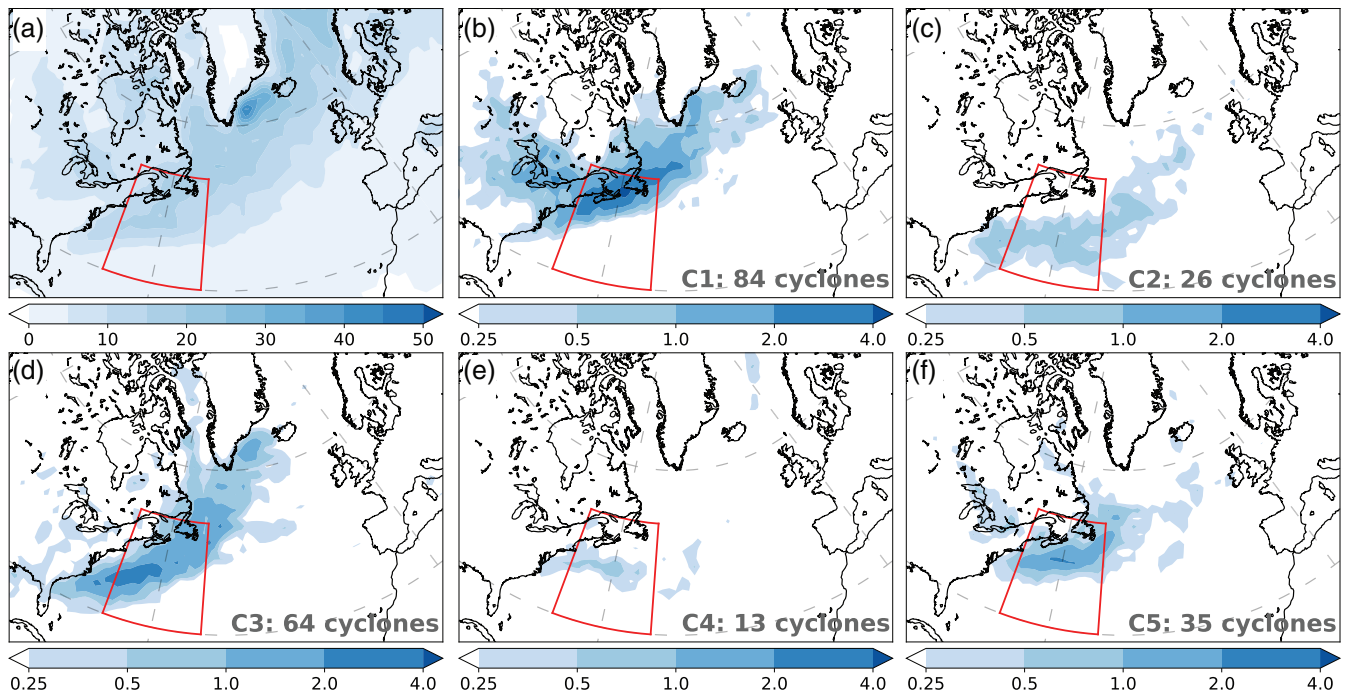


FIGURE 2 (a) Cyclone density (10^{-6} km^{-2}) based on the ERA-Interim reanalysis for the winter seasons in 1979–2016. (b)–(f) are as (a) but for cyclones with maximum intensification in the Gulf Stream region in categories C1 to C5, respectively. See main text for more details on the cyclone detection and categorisation

but more variable distribution, due to the lower number of cyclones than in C1 and C3. Following the definition of Sanders and Gyakum (1980), 40% of the cyclones in C3 (26 cyclones), 23% of the cyclones in C1 (19 cyclones), and only 11% of the cyclones in C2 (3 cyclones) are explosively developing cyclones. The total number of explosive cyclones is smaller than in the climatologies of Lim and Simmonds (2002) and Allen *et al.* (2010), as we restrict our analysis to the Gulf Stream region.

The location of maximum intensification is equally spread on the cold and warm sides of the SST front for categories C1 and C2, while the locations are spread along the main SST gradient for C3 (Figure 4a–c). For C1, and in particular C3, the location of maximum intensity is close to the location of maximum intensification. In contrast, cyclones of C2 reach their maximum intensity further downstream.

3.2 | Cyclone-relative SST and wind composites

We present cyclone-relative composites for C1, C2, and C3 to clarify the potential role of the SST front, the land–sea contrast, and upper-level forcing on the cyclone structure and intensity. Cyclone centres in the composites represent the minimum sea level pressure. In the following, we will contrast the non-crossing categories C1 and C2

with the crossing category C3. We present composites for the time of maximum intensification (centre column in Figures 5–9) as well as 12 hr before and after this time (left and right columns in Figures 5–9, respectively).

Due to the cyclones in C1 moving towards higher SSTs (Figures 2b and 3a), we observe an increase in SST with time in the southeastern quadrant before the time of maximum intensification (Figure 5a,b). Due to the southern position of cyclones in C2 (Figure 2c), they are propagating over higher SSTs than in C1. In contrast to C2 (Figure 5d–f), cyclones in C1 are associated with the strongest temperature gradient at 850 hPa, most likely due to the proximity of the cyclones to the United States east coast throughout their evolution (Figure 5a–c). However, in both categories there is a gradual increase of the maximum wind speed at 925 hPa from 18 m s^{-1} at 12 hr prior to maximum intensification to 24 m s^{-1} 24 hr later (Figure 5a–c,d–f), with the maximum wind speed observed in the southeastern quadrant, due to the superposition of the cyclonic circulation and the eastward propagation.

Twelve hours prior to their maximum intensification, cyclones of C3 are located on the warm side of the SST front, similar to cyclones of C2. However, cyclones of C3 propagate closer to both the SST front and the landmass (Figures 3a and 5g), which likely explains the stronger temperature gradient at 850 hPa observed in C3 than in C2. Drawing air both from the warm side of the SST front and the cold continent, cyclones of C3 can make use of the

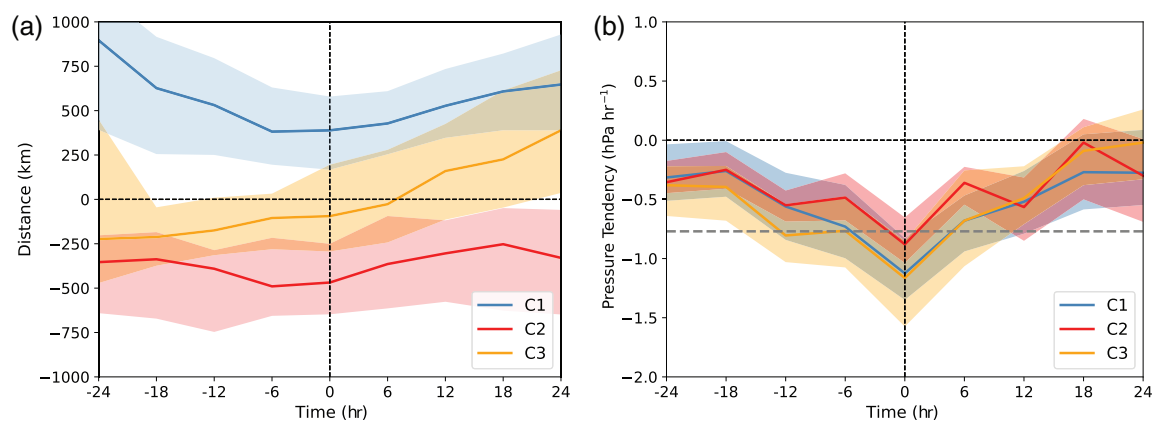


FIGURE 3 (a) Distance (km) between cyclone centres and the SST front relative to the time of maximum intensification. Lines indicate the 50th percentile and the shading the interquartile range. (b) is as (a), but for the pressure tendency ($\text{hPa}\cdot\text{hr}^{-1}$)

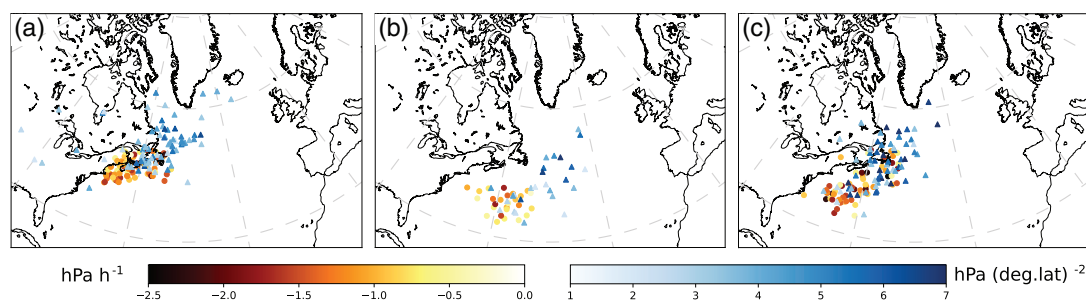


FIGURE 4 Locations of cyclone maximum intensification ($\text{hPa}\cdot\text{h}^{-1}$, yellow-red circles) and cyclone maximum intensity ($\text{hPa}\cdot(\text{deg}\cdot\text{lat})^{-2}$, blue triangles) for category (a) C1, (b) C2, and (c) C3

combined thermal gradient across both the SST front and the coastline. This interpretation is in line with Brayshaw *et al.* (2009), who documented increased near-surface low-level baroclinicity along the United States east coast, where the cold dry continental air meets the warmer and moist air over the ocean.

Contrary to C1, the SST decreases with time for C3, consistent with the propagation towards the cold side of the SST front (Figures 2d and 5g–i). As for C1 and C2, the wind speed increases with time for C3 (Figure 5g–i), and the highest wind speed, exceeding $30\text{ m}\cdot\text{s}^{-1}$, is observed 12 hr after maximum intensification (Figure 5i). The wind decays 18 hr after the maximum intensification (not shown).

3.3 | Cyclone-relative surface heat flux composites

For both C1 and C2, the latent heat fluxes are always upward (Figure 6a–c,d–f) and largest in the southwestern quadrant south of the SST front due to the increase in surface saturation mixing ratio with increasing SST.

Likewise, sensible heat fluxes are directed towards the atmosphere in the southwestern quadrant, within the cyclone's cold sector (Figure 6a–c,d–f). Both fluxes are highest south of the SST front due to an increase in SST (consistent with, e.g., Zolina and Gulev, 2003; Vanni re *et al.*, 2017a). Twelve hours before maximum intensification, there are on average significantly lower fluxes for C1 than for C2. This is most likely associated with the propagation of the C2 cyclones over higher SSTs than for C1 (Figure 2b,c). However, for both categories, there is a marked increase in both latent and sensible heat fluxes in the southwestern quadrant within 24 hr (Figure 6a–c,d–f) associated with the proximity of the SST front. Consistent with Businger *et al.* (2005) and Rudeva and Gulev (2011), the maximum sensible and latent heat fluxes are almost collocated, with a slight northward shift of the sensible heat fluxes compared to the latent heat fluxes. Similar to C1, surface heat fluxes increase within the 24 hr period (Figure 6d–f).

C3 can be considered a combination of C1 and C2, as cyclones are initially located on the warm side of the SST front (C2) before crossing to the cold side (C1). At 12 hr before maximum intensification, latent and sensible

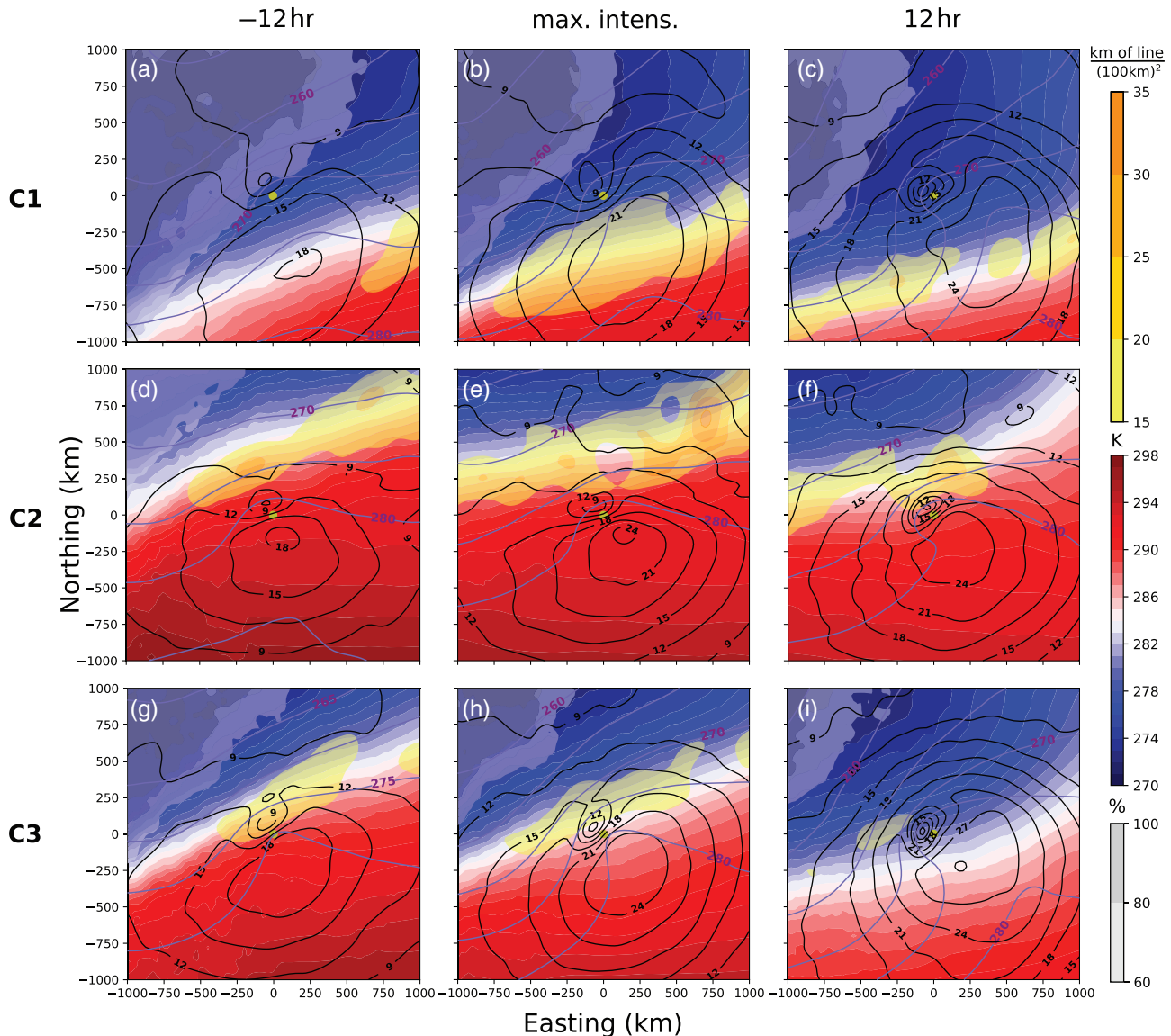


FIGURE 5 Composite evolution of cyclone-centred SST (blue-red shading, K), temperature at 850 hPa (purple contours with interval 5 K), wind speed at 925 hPa (black contours with interval $3 \text{ m}\cdot\text{s}^{-1}$), SST front density (yellow shading, in 10^{-5} km^{-1}) and probability of being over land (grey shading, 60–100%). (a, d, g) are at 12 hr prior to maximum intensification, (b, e, h) at maximum intensification, and (c, f, i) at 12 hr after maximum intensification, for categories (a–c) C1, (d–f) C2, and (g–i) C3

heat fluxes are relatively high, exceeding $240 \text{ W}\cdot\text{m}^{-2}$ and $100 \text{ W}\cdot\text{m}^{-2}$, respectively (Figure 6g). These values are higher than for C2 (Figure 6d), because the cyclones are located closer to the SST front (Figure 3a) and the wind is stronger (Figure 5d,g). Similar to C1, C3 consists of cyclone tracks located closer to the continent at the early stage of development (Figure 2b,d) and are thus more strongly influenced by cold continental air masses (Figure 5d,g) than C2.

During maximum intensification, sensible (latent) heat fluxes increased to more than 100 (160) $\text{W}\cdot\text{m}^{-2}$ for C1 (Figure 6b). Twelve hours past maximum intensification, upward sensible heat fluxes increased to approximately $160 \text{ W}\cdot\text{m}^{-2}$ in the southwestern quadrant (Figure 6c).

Besides that, downward sensible heat fluxes appear in the eastern quadrant due to warm air advection over relatively lower SST (Figure 6b,c), yielding a dipole structure in the sensible heat flux, with positive values to the west and negative sensible heat fluxes to the east (consistent with Rudeva and Gulev, 2011; Dacre *et al.*, 2020). This tongue of warm air is wrapped cyclonically around the cyclone centre. For C3, the heat fluxes (Figure 6h,i) are equivalent to C1 (Figure 6b,c) with a similar dipole emerging in the sensible heat fluxes 12 hr after maximum intensification (Figure 6i).

In C2, this dipole in sensible heat fluxes is much less pronounced, because these cyclones generally form further away from the North American continent than

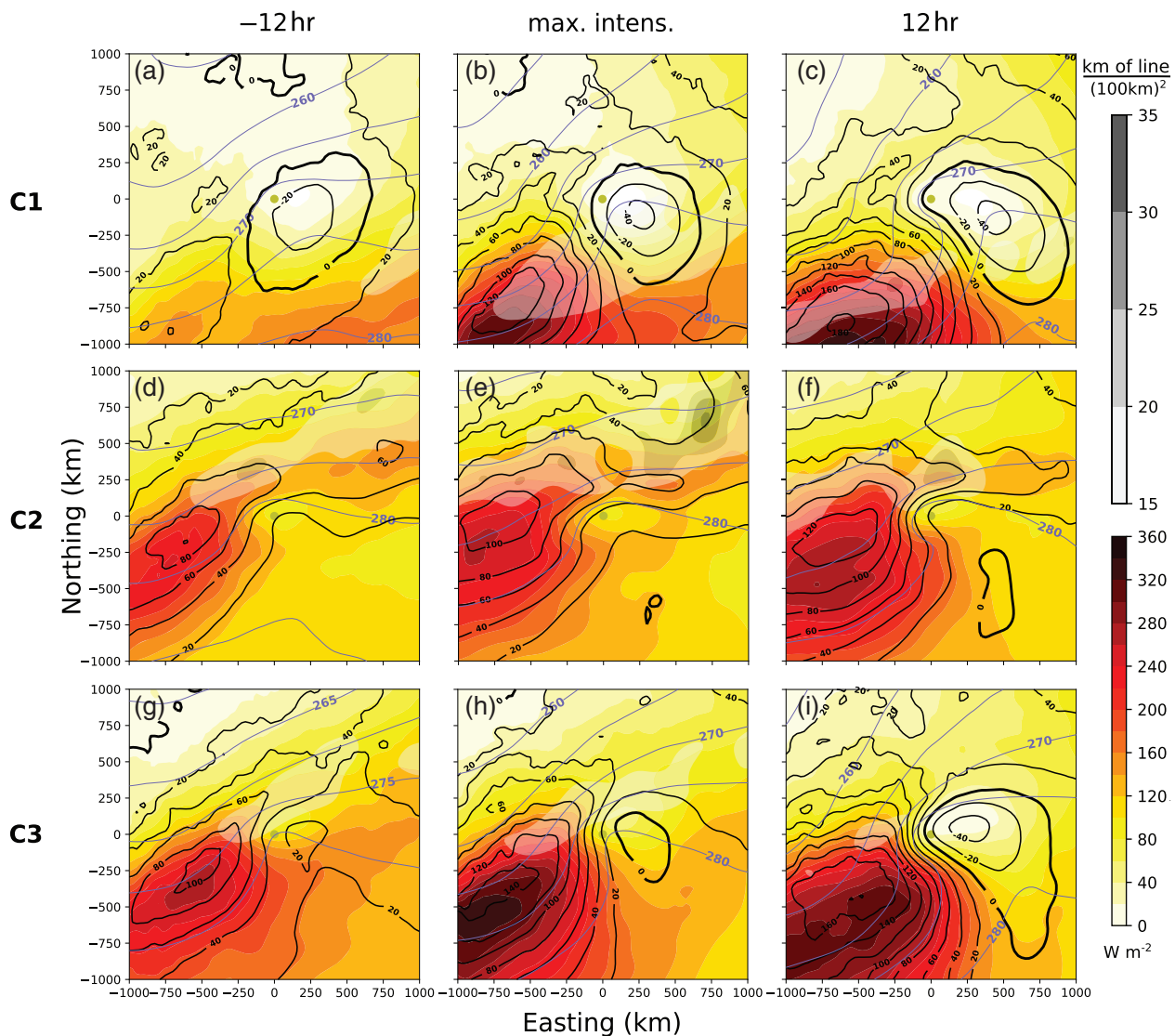


FIGURE 6 As Figure 5, but showing evolution of cyclone-centred latent heat fluxes (yellow-red shading, $\text{W}\cdot\text{m}^{-2}$), sensible heat fluxes (black contours with interval $20\text{ W}\cdot\text{m}^{-2}$, with thick line for zero), and temperature at 850 hPa (purple contours with interval 5 K). Here, SST front density is shown as grey shading

those in C1 and C3 (Figure 5). The surface upward heat fluxes slightly increase with time (Figure 6e,f), but only weak downward sensible heat fluxes appear 12 hr after maximum intensification (Figure 6f). This is due to both the warm airstream not crossing the SST front (Figure 6f) and the tongue of warm air wrapped around the cyclone centre being less pronounced for C2 than for C1 and C3.

3.4 | Cyclone-relative moisture and precipitation composites

C2 is characterised by higher values of TCWV, exceeding $30\text{ kg}\cdot\text{m}^{-2}$, and stronger moisture transport (Figure 7d–f) than C1 (Figure 7a–c). The increase of TCWV with SST

is expected from the Clausius–Clapeyron relation, as cyclones in C2 propagate towards the warm and moist side of the SST front. The maximum values of TCWV for C2 occur 12 hr before maximum intensification (Figure 7d). Thereafter, the values slightly decrease with time as the cyclones propagate to the northeast towards lower SSTs. Nonetheless, TCWV remains relatively high ($>27\text{ kg}\cdot\text{m}^{-2}$) throughout the evolution as the cyclones remain on the warm side of the SST front (Figure 7e,f).

In contrast, cyclones of C1 remain on the cold side of the SST front, propagate over lower SSTs (Figure 7a–c) and are thus associated with lower TCWV. However, higher values of TCWV in excess of $27\text{ kg}\cdot\text{m}^{-2}$ appear during maximum intensification (Figure 7b) compared to 12 hr before (Figure 7a), located approximately 750 km to the south of the cyclone centre. We associate the maximum values

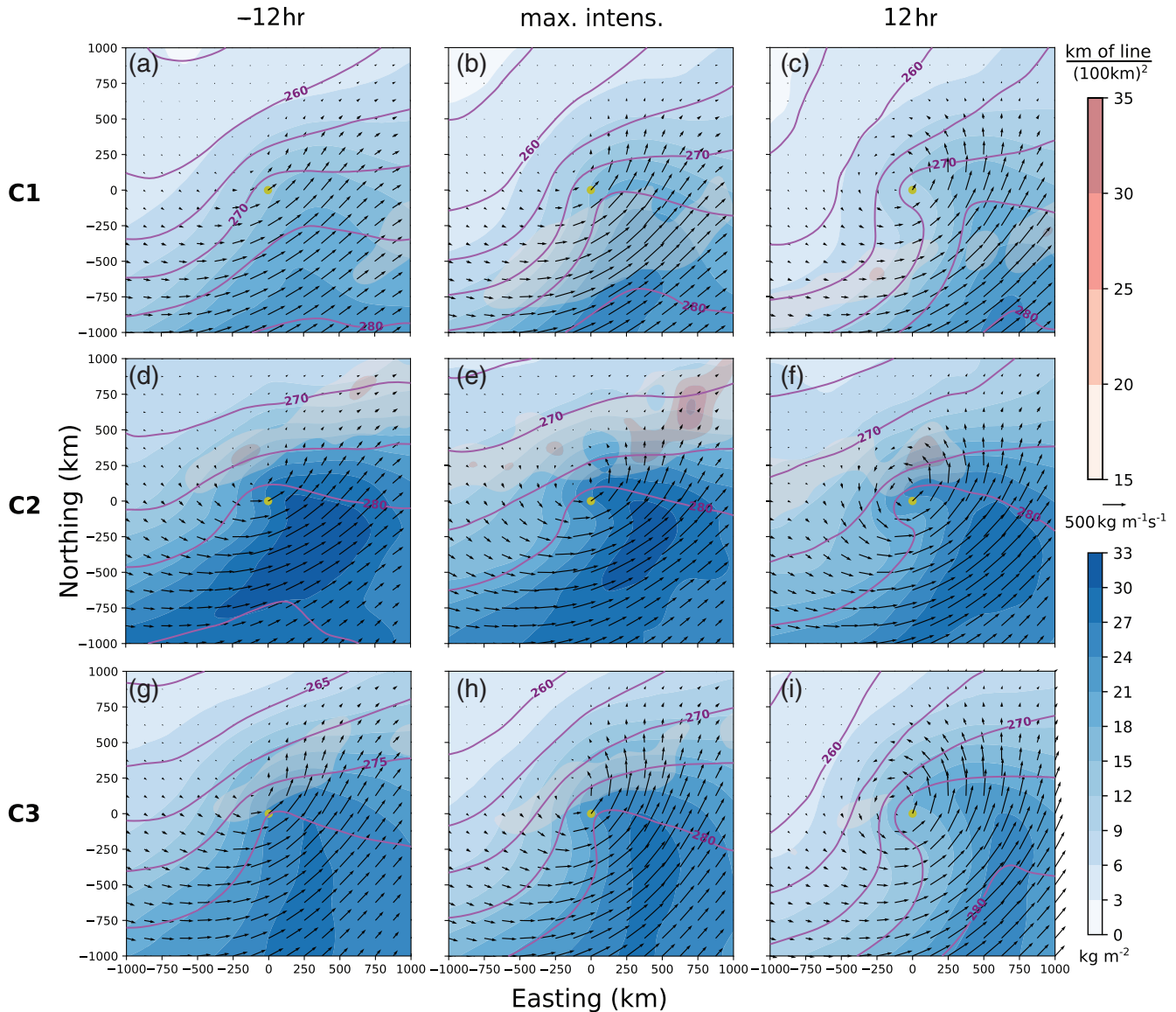


FIGURE 7 As Figure 5, but showing evolution of cyclone-centred total column water vapour (blue shading, $\text{kg}\cdot\text{m}^{-2}$), integrated water vapour flux (black vectors), and temperature at 850 hPa (purple contours with interval 5 K). Here, SST front density is shown as pink shading

of TCWV, during the maximum intensification with the smaller distance between the cyclones and the SST front (Figure 3a), which enables moisture uptake from the warm side of the SST front.

For both C1 and C2, the moisture transport increases in the 12 hrs before the time of maximum intensification (Figure 7a,b,d,e). At the time of maximum intensification, the transport peaks around 400–500 km to the south-southeast of the cyclone core (Figure 7b,e). At 12 hr after maximum intensification, the strong moisture transport persists, but occurs at a greater distance, approximately 600 km southeast of the cyclone centre (Figure 7c,f). The cyclonic wrap-up of the warm sector is also evident in TCWV as well as the moisture transport for both C1 and C2, though more distinctly for C2 (Figure 7f).

Both C1 and C2 are characterised by similar average large-scale precipitation. For C1, large-scale precipitation increases gradually throughout the cyclone evolution (Figure 8a–c). For C2, large-scale precipitation rate is generally higher (Figure 8d–f) than for C1 (Figure 8a–c), however the average large-scale precipitation rate is similar to C1, despite the higher availability of moisture (compare Figure 7d–f with Figure 7a–c). Based on the 925 hPa wind speeds for the two categories, we conclude that the cyclones of the two categories are rather similar, in terms of intensity. Surprisingly though, they result in the same amount of precipitation, which could be due to the isentropic ascent of the baroclinic moisture flux that leads to higher precipitation (McTaggart-Cowan *et al.*, 2017). Based on the larger temperature gradient in C1

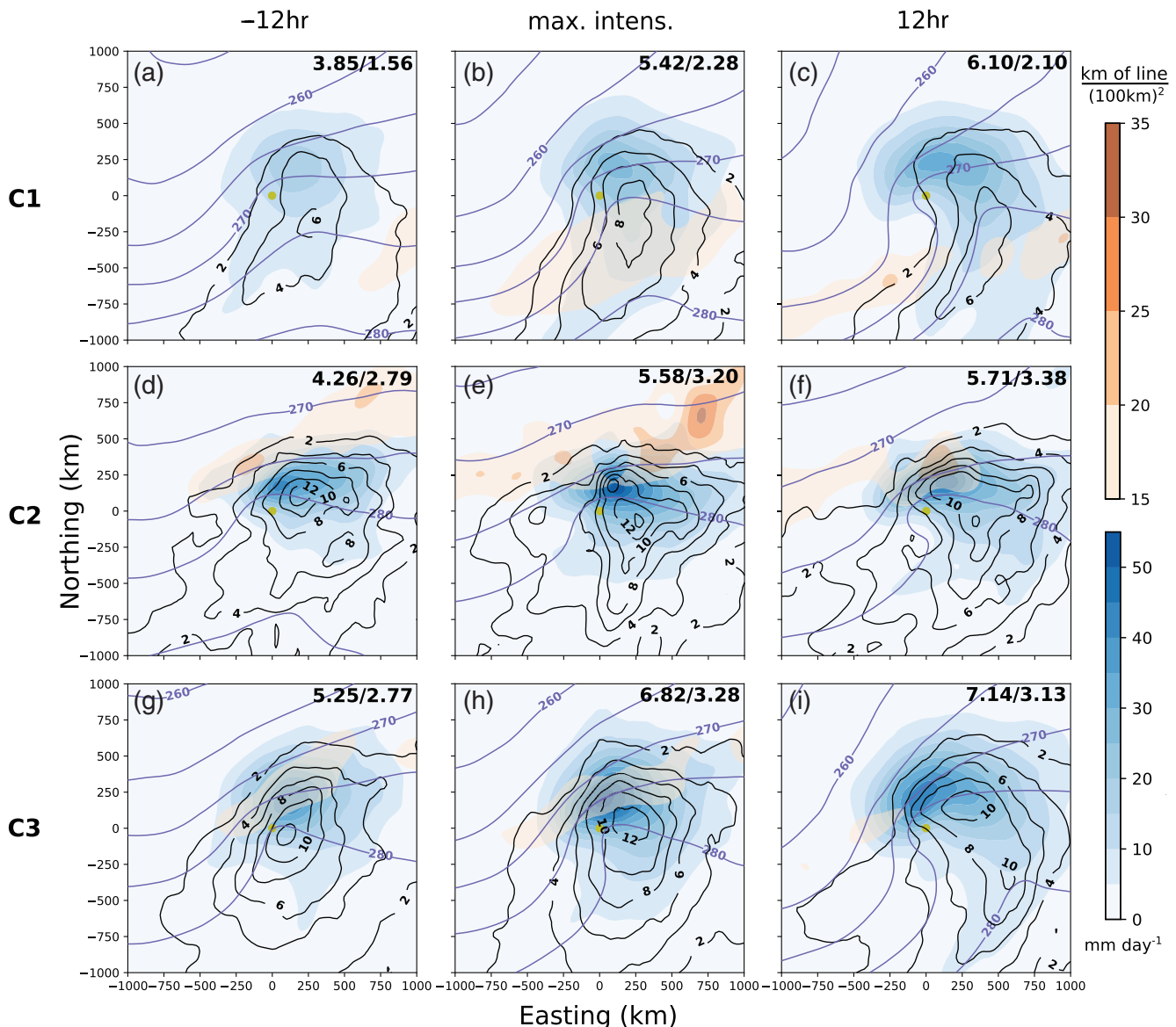


FIGURE 8 As Figure 5, but showing evolution of cyclone-centred large-scale precipitation rate (blue shading, $\text{mm}\cdot\text{day}^{-1}$), convective precipitation rate (black contours, $\text{mm}\cdot\text{day}^{-1}$), and temperature at 850 hPa (purple contours with interval 5 K). Here, SST front density is shown as orange shading. Numbers in the top right of each panel represent the average large-scale/convective precipitation rate in the composite domain in $\text{mm}\cdot\text{day}^{-1}$

(Figure 5a–c) than in C2 (Figure 5d–f), we hypothesise that the increased isentropic upglide in C1 indeed results in more precipitation compared to the sole contributions of cyclone intensity and moisture availability, as described in Pfahl *et al.* (2015).

Conversely, the convective precipitation for C2 is higher (Figure 8d–f) than for C1 (Figure 8a–c), due to higher TCWV (Figure 7d–f) and higher SSTs (compare Figure 5d–f with Figure 5a–c). For both C1 and C2, the highest convective precipitation rate coincides with the time of maximum intensification (Figure 8b,e), exceeding $14\text{ mm}\cdot\text{day}^{-1}$ for C2. A maximum of convective precipitation is observed during maximum intensification for

C1, when cyclones are typically closer to the SST front (Figure 3a) and thus reside in a region with higher SSTs (Figure 5b) and moisture (Figure 7b) than 12 hr previously and subsequently (Figure 5a,c). For C2, the cyclones always stay on the warm and moist side of the SST front and thus it is the increase in intensity that increases convective precipitation.

Structurally, precipitation occurs in a relatively broad region tracing the cyclone's cold front in C1, whereas it is more confined within the cyclone core in C2 (Figure 8a–f). These structural differences of the cyclone are in line with the findings of Pfahl *et al.* (2015), who compared the structure of cyclones in warmer and colder climates. Therefore,

the difference in the spatial distribution of precipitation most likely arises due to the higher SST in C2 (Figure 5f) than in C1 (Figure 5c).

The decrease of TCWV with time in C3 is consistent with the gradual propagation of cyclones over lower SSTs. Maximum values of TCWV exceed $27 \text{ kg}\cdot\text{m}^{-2}$ up to the time of maximum intensification and are located to the southeast of the cyclone core within the cyclone's warm sector (Figure 7g,h). They decrease slightly until 12 hr after maximum intensification when cyclones propagate towards the cold side of the SST front (Figure 7i). This evolution and location of the maximum values of TCWV is similar to C1 and C2 (Figure 7b,e). However, the maximum values of TCWV are observed in a south–north direction and not from the southwest to the northeast as in C1 and C2. Consistent with the TCWV, the largest moisture transport also occurs to the southeast of the cyclone core and has again a more meridional component, contrary to C1 and C2, where the transport is oriented from the southwest to the northeast.

Similar to C2, the strongest convective precipitation in C3 occurs during maximum intensification (Figure 8h). At this point in time, cyclones in C3 are propagating over regions of higher SSTs and, based on the higher wind speed (Figure 5g,h), are stronger than at 12 hr prior to maximum intensification. At 12 hr after maximum intensification, convective precipitation is reduced, in line with the cyclones propagating over lower SSTs (Figure 5i) compared to 12 hr before (Figure 5h). Thus, more rapidly intensifying cyclones propagating over regions with higher SSTs are associated with higher convective precipitation.

Cyclones in C3 are associated with the highest average large-scale precipitation (Figure 8g–i) rate among the three categories, with the maximum average large-scale precipitation rate of $7.14 \text{ mm}\cdot\text{day}^{-1}$ occurring 12 hr after maximum intensification. The distribution of large-scale precipitation in C3 (Figure 8g–i) is similar to C1 (Figure 8a–c), affecting a broader area around the cyclone core, which is different from the locally confined distribution in C2 (Figure 8d–f). The fact that cyclones in C1 and C3 propagate over regions with lower SSTs (Figure 6c,i) than in C2 (Figure 6f) during this later stage of development further supports the connection between the SST and the spatial distribution of precipitation. The observation that C3 features the highest precipitation is also consistent with the higher intensification (Figures 3b and 8i), high wind speed (Figure 5i), and stronger surface heat fluxes (Figure 6i) than in the other categories.

Contrary to C1 and C2, the maximum of large-scale precipitation for C3 at 12 hr after maximum intensification is located to the north-northwest of the cyclone core (Figure 8i), which is consistent with the more wrapped-up structure of the cyclones in C3 than in C1 and C2 (compare

Figures 6c,f,i). This structure indicates a faster development of cyclones in C3, consistent with cyclones reaching their maximum intensity sooner after their maximum intensification than in the other categories (Figure 4a–c). Given that all cyclones passed their time of maximum intensification, it is likely that they feature an occlusion, which is commonly associated with a maximum in precipitation (Sanders, 1986; Martin, 1998). The more rapid wrap-up and occlusion process in C3 than in C1 and C2 explains the increased precipitation.

Overall, the features in large-scale precipitation for C3 can be seen as a combination of C1 and C2. For C1, we concluded that the larger temperature gradient than in C2 mainly explains the increased precipitation, whereas for C2 it is mainly the higher values of TCWV that contribute to the increased precipitation. With both cyclone strength and moisture availability resulting in increased large-scale precipitation (Pfahl and Sprenger, 2016), it is straightforward that C3 has higher values than C1 and C2 due to the cyclones in C3 being both stronger (Figure 5g–i) and featuring higher TCWV (Figure 7g–i) than C1 and C2.

3.5 | Cyclone-relative geopotential and wind at 300 hPa

Cyclones in C2 evolve at a greater distance from the climatological position of the North Atlantic jet compared to the other categories (Figures 1a and 2b–d). Consistently, cyclones of C2 are associated with the lowest wind speed maximum at 300 hPa during maximum intensification (Figure 9e). The structure in the geopotential field indicates a gradual development of an upper-level trough in the northwest quadrant and a corresponding shift in the position of the wind maximum to the south (Figure 9d–f).

Compared to C2, cyclones of C1 and C3 propagate at a smaller distance from the North Atlantic jet (Figures 1a and 2b,d). Consequently, the isohypses are distributed tighter than in C2 (Figure 9a–c,g–i) and feature a jet streak of $50\text{--}60 \text{ m}\cdot\text{s}^{-1}$ to the southwest of the cyclone centre. While all categories are associated with a trough at 300 hPa, this trough is much more pronounced in C1 and C3 than in C2 (Figure 9).

Cyclones in C1 are associated with the strongest jet and most pronounced upper-level trough among the three categories, with cyclones being located near the left exit of the jet (Figure 9a–c), a position favourable for the increase of large-scale precipitation via forced ascent (e.g., Johnson and Daniels, 1954; Brown *et al.*, 1994; Milrad, 2017). The upper-level forcing is thus a plausible explanation for why cyclones in C1 and C2 produce a similar area-averaged precipitation rate (Figure 8a–f), although considerably more moisture is available for C2

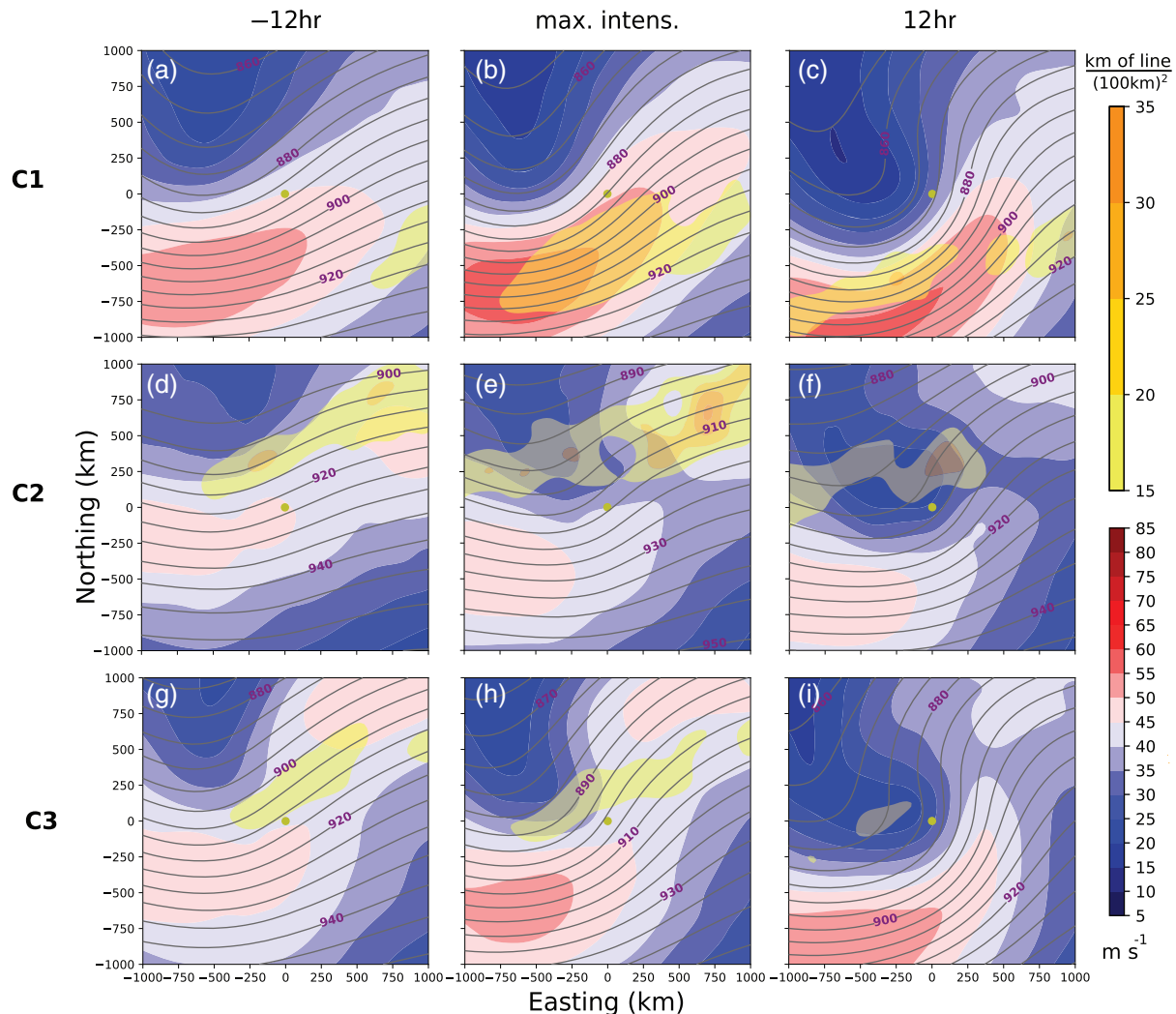


FIGURE 9 As Figure 5, but showing evolution of cyclone-centred SST front density (yellow shading, in 10^{-5}km^{-1}), wind speed at 300 hPa (blue-red shading, $\text{m}\cdot\text{s}^{-1}$) and geopotential height at 300 hPa (grey contours with interval 5 gpm). Here, SST front density is shown as yellow shading

(Figure 7a–f). We thus confirm the previously highlighted (e.g., Uccellini, 1990; Riviere and Joly, 2006; Milrad, 2017) contribution of the upper-level forcing to cyclone intensification and increased average large-scale precipitation rate for cyclones in C1. The average large-scale precipitation rate in C2 can be related to the higher moisture availability, in line with previous studies (e.g., Field and Wood, 2007; Pfahl and Sprenger, 2016).

4 | DISCUSSION AND CONCLUDING REMARKS

We classified cyclones in the Gulf Stream region with respect to their propagation relative to the SST front, which we detected automatically using an established algorithm that was originally developed to identify atmospheric front

lines. We considered cyclones which stay either on the cold (C1) or warm (C2) side of the SST front, and those crossing the SST front from the warm to the cold side (C3). A high density of cyclone tracks associated with the North Atlantic storm track (Figure 2a) coincides with the region of the highest SST front density (Figure 1a). To compare the characteristics of cyclones following different tracks relative to the SST front, we performed a composite analysis around the time of maximum intensification. We use composites to analyse the respective roles of the SST front, the land–sea contrast, and the upper-level forcing on cyclone development.

Cyclones in C1 and C3 intensify more rapidly than cyclones in C2 (Figure 3b). Cyclones in C1 and C3 frequently form over land (Figure 2b–d) and propagate closer to the continent during their evolution than cyclones in C2 (Figure 5). Thus, they commonly include continental

air masses in their cold sector (Figure 5a,g). The continental air mass provides additional baroclinicity which is conducive for cyclone intensification. Cyclones in C1 propagate closer to the land, yet at a greater distance from the SST front than cyclones in C3. However, for most of the evolution, low-level baroclinicity is lower around C3 cyclones than around C1 cyclones. This comparison between C1 and C3 suggests that the role of the SST front is secondary compared to that of the land–sea contrast for the low-level baroclinicity. Nevertheless, cyclones of C3 deepen most rapidly on average and feature the highest fraction of explosive cyclones. Based on the rather similar orientation of the upper-level wave in C1 and C3, we relate the more rapid intensification for cyclones in C3 to the increased latent heat release within the cyclones' warm conveyor belt, as cyclones in C3 are associated with the highest average large-scale precipitation rate among the three categories (Figure 8).

Contrary to cyclones of C1 and C3, cyclones of C2 remain distant from both the SST front and the continent (Figures 2c and 5d–f) resulting in a less pronounced temperature gradient across the cyclone. In addition, C2 cyclones are typically furthest away from the upper-level jet and associated with the least pronounced trough. They thus receive considerably less upper-level forcing than C1 and C3 cyclones, which both develop in the left exit region of a pronounced jet.

Cyclones for all categories reach their maximum surface heat fluxes 12 hr after their maximum intensification (Figure 6c,f,i), the time when they tend to reach their maximum intensity. Cyclones of C1 and C3 are associated with a pronounced dipole structure in the sensible heat flux, with positive (negative) values to the west (east) of the cyclone core, which is absent for cyclones of C2 (Figure 6a–c,h,i). This dipole structure is detrimental to cyclone intensification as it reduces baroclinicity and thus available potential energy in the cyclone. However, cyclones of C1 and C3 are still associated with a higher intensification than cyclones in C2 (Figure 3b). Thus, the intensification of cyclones is not directly associated with the surface heat fluxes. Instead, the strength of the surface fluxes is closely tied to the different pathways of the cyclones and in particular the proximity to the SST front and the cold continent.

We find convective precipitation to be closely related to the SSTs under the cyclone. For example, convective precipitation is strongest for C2, in which the cyclones propagate over the highest SSTs (Figure 5d–f). Further, for C3, convective precipitation evolves parallel to the SSTs. Before maximum intensification (Figure 8d,e,g,h), SSTs and convective precipitation are both most intense, and both decrease in tandem with the cyclone crossing the SST fronts. As this relation between SSTs and convective precipitation holds for all our categories, we conclude that

convective precipitation is strongly modulated by the absolute SST, independent of whether or not the cyclones cross the SST front.


Strongest average large-scale precipitation is associated with cyclones in C3. Cyclones in this category are the most intense as measured by 925 hPa wind speeds, and have available nearly as much moisture as cyclones in C2. However, the average large-scale precipitation for C1 and C2 are rather similar, despite the larger moisture availability in C2 (Figure 8a–f). Thus, C2 seems to be less efficient than C1 in making use of the available moisture. We identified two likely reasons for this reduced efficiency. First, cyclones in C1 intensify more due to considerably stronger upper-level forcing than in C2. Second, temperature gradients across C2 cyclones are smaller than across C1 cyclones, which implies a reduced isentropic upglide. We consequently hypothesize that low-level baroclinicity might be an additional factor determining precipitation intensity, in addition to moisture availability and cyclone intensity as documented by Pfahl and Sprenger (2016). Our hypothesis is supported by McTaggart-Cowan *et al.* (2017) who document that the strongest precipitation in a cyclone is co-located with the strongest moist isentropic upglide.

Overall, we identified that the land–sea contrast has a clear influence on cyclone intensification in the Gulf Stream region for cyclones staying to the north of the SST front (C1) through increased low-level baroclinicity. For cyclones crossing the SST front from the warm to the cold side (C3), low-level baroclinicity is slightly weaker than in C1, but is nevertheless attributable to both the land–sea contrast and the SST front. Furthermore, both C1 and C3 are associated with stronger upper-level forcing, which contributes to cyclone intensification in addition to the low-level baroclinicity. However, given the specific geographic features of the western North Atlantic, a generalisation of our results to SST fronts associated with other western boundary currents is not straightforward. Therefore, a similar study should be conducted for the Kuroshio Extension region. The cold continental air masses in the West Pacific are located further away from the SST front than in the Gulf Stream region. This would allow us to further assess the relative role of the land–sea contrast and the SST front for cyclone intensification in these two regions with the strongest western boundary currents in the Northern Hemisphere.

ORCID

Leonidas Tsoupiridis  <https://orcid.org/0000-0002-2043-0871>

Clemens Spensberger  <https://orcid.org/0000-0002-9649-6957>

Thomas Spengler  <https://orcid.org/0000-0002-1747-6385>

REFERENCES

- Allen, J.T., Pezza, A.B. and Black, M.T. (2010) Explosive cyclogenesis: A global climatology comparing multiple reanalyses. *Journal of Climate*, 23, 6468–6484.
- Berry, G., Reeder, M.J. and Jakob, C. (2011) A global climatology of atmospheric fronts. *Geophysical Research Letters*, 38, L04809.
- Booth, J.F., Naud, C.M. and Willison, J. (2018) Evaluation of extratropical cyclone precipitation in the North Atlantic basin: An analysis of ERA-Interim, WRF, and two CMIP5 models. *Journal of Climate*, 31, 2345–2360.
- Booth, J.F., Thompson, L., Patoux, J. and Kelly, K.A. (2012) Sensitivity of midlatitude storm intensification to perturbations in the sea surface temperature near the Gulf Stream. *Monthly Weather Review*, 140, 1241–1256.
- Brayshaw, D.J., Hoskins, B.J. and Blackburn, M. (2009) The basic ingredients of the North Atlantic storm track. Part I: Land–sea contrast and orography. *Journal of the Atmospheric Sciences*, 66, 2539–2558.
- Brown, R.H., Baker, D.J. and Friday, E.W. (1994) *The Great Flood of 1993*. Natural disaster survey report, NOAA National Weather Service, Silver Spring, MD.
- Businger, S., Graziano, T.M., Kaplan, M.L. and Rozumalski, R.A. (2005) Cold-air cyclogenesis along the Gulf Stream front: Investigation of diabatic impacts on cyclone development, frontal structure, and track. *Meteorology and Atmospheric Physics*, 88, 65–90.
- Catto, J. (2016) Extratropical cyclone classification and its use in climate studies. *Reviews of Geophysics*, 54, 486–520.
- Cione, J.J., Raman, S. and Pietrafesa, L.J. (1993) The effect of Gulf Stream-induced baroclinicity on U.S. East Coast winter cyclones. *Monthly Weather Review*, 121, 421–430.
- Dacre, H.F., Josey, S.A. and Grant, A.L. (2020) Extratropical cyclone induced sea surface temperature anomalies in the 2013/14 winter. *Weather and Climate Dynamics*, 1, 27–44.
- de Vries, H., Scher, S., Haarsma, R., Drijfhout, S. and Van Delden, A. (2019) How Gulf Stream SST-fronts influence Atlantic winter storms. *Climate Dynamics*, 52, 5899–5909.
- Dee, D.P., Uppala, S.M., Simmons, A.J., Berrisford, P., Poli, P., Kobayashi, S., Andrae, U., Balmaseda, M.A., Balsamo, G., Bauer, P., Bechtold, P., Beljaars, A.C.M., van de Bergd, L., Bidlot, J., Bormann, N., Delsol, C., Dragani, R., Fuentes, M., Geer, A.J., Haimberger, L., Healy, S.B., Hersbach, H., Holm, E.V., Isaksen, I., Kållberg, P., Köhler, M., Matricardi, M., McNally, A.P., Monge-Sanz, B.M., Morcrette, J.-J., Park, B.-K., Peubey, C., de Rosnay, P., Tavolato, C., Thépaut, J.-N. and Vitart, F. (2011) The ERA-Interim reanalysis: configuration and performance of the data assimilation system. *Quarterly Journal of the Royal Meteorological Society*, 137, 553–587.
- Evans, M.S., Keyser, D., Bosart, L.F. and Lackmann, G.M. (1994) A satellite-derived classification scheme for rapid maritime cyclogenesis. *Monthly Weather Review*, 122, 1381–1416.
- Field, P.R. and Wood, R. (2007) Precipitation and cloud structure in midlatitude cyclones. *Journal of Climate*, 20, 233–254.
- Hanley, J. and Caballero, R. (2012) The role of large-scale atmospheric flow and Rossby wave breaking in the evolution of extreme windstorms over Europe. *Geophysical Research Letters*, 39(21). <https://doi.org/10.1029/2012GL053408>.
- Hawcroft, M.K., Shaffrey, L.C., Hodges, K.I. and Dacre, H.F. (2012) How much Northern Hemisphere precipitation is associated with extratropical cyclones?. *Geophysical Research Letters*, 39(24). <https://doi.org/10.1029/2012GL053866>.
- Hewson, T.D. (1998) Objective fronts. *Meteorological Applications*, 5, 37–65.
- Hodges, K.I., Lee, R.W. and Bengtsson, L. (2011) A comparison of extratropical cyclones in recent reanalyses ERA-Interim, NASA MERRA, NCEP CFSR, and JRA-25. *Journal of Climate*, 24, 4888–4906.
- Hoskins, B.J. and Hodges, K.I. (2002) New perspectives on the Northern Hemisphere winter storm tracks. *Journal of the Atmospheric Sciences*, 59, 1041–1061.
- Hotta, D. and Nakamura, H. (2011) On the significance of sensible heat supply from the ocean in the maintenance of mean baroclinicity along storm tracks. *Journal of Climate*, 24, 3377–3401.
- Inatsu, M., Mukougawa, H. and Xie, S.-P. (2000) Formation of subtropical westerly jet core in an idealized GCM without mountains. *Geophysical Research Letters*, 27, 529–532.
- Inatsu, M., Mukougawa, H. and Xie, S.-P. (2003) Atmospheric response to zonal variations in midlatitude SST: Transient and stationary eddies and their feedback. *Journal of Climate*, 16, 3314–3329.
- Jacobs, N., Raman, S., Lackmann, G. and Childs, P.Jr. (2008) The influence of the Gulf Stream induced SST gradients on the US East Coast winter storm of 24–25 January 2000. *International Journal of Remote Sensing*, 29, 6145–6174.
- Jenkner, J., Sprenger, M., Schwenk, I., Schwierz, C., Dierer, S. and Leuenberger, D. (2010) Detection and climatology of fronts in a high-resolution model reanalysis over the Alps. *Meteorological Applications*, 17, 1–18.
- Johnson, D. and Daniels, S. (1954) Rainfall in relation to the jet stream. *Quarterly Journal of the Royal Meteorological Society*, 80, 212–217.
- Kuo, Y.-H., Shapiro, M.A. and Donall, E.G. (1991) The interaction between baroclinic and diabatic processes in a numerical simulation of a rapidly intensifying extratropical marine cyclone. *Monthly Weather Review*, 119, 368–384.
- Lee, T. and Cornillon, P. (1996) Propagation and growth of Gulf Stream meanders between 75° and 45°W. *Journal of Physical Oceanography*, 26, 225–241.
- Lim, E.-P. and Simmonds, I. (2002) Explosive cyclone development in the Southern Hemisphere and a comparison with Northern Hemisphere events. *Monthly Weather Review*, 130, 2188–2209.
- Manobianco, J. (1988) *On the observational and numerical aspects of explosive east coast cyclogenesis*. Report No. 88-7, Department of Meteorology, Florida State University, Tallahassee, FL.
- Manobianco, J. (1989) Explosive East Coast cyclogenesis over the west-central North Atlantic Ocean: A composite study derived from ECMWF operational analyses. *Monthly Weather Review*, 117, 2365–2383.
- Martin, J.E. (1998) The structure and evolution of a continental winter cyclone. Part II: Frontal forcing of an extreme snow event. *Monthly Weather Review*, 126, 329–348.
- McTaggart-Cowan, R., Gyakum, J.R. and Moore, R.W. (2017) The baroclinic moisture flux. *Monthly Weather Review*, 145, 25–47.
- Meinen, C.S. and Luther, D.S. (2016) Structure, transport, and vertical coherence of the Gulf Stream from the Straits of Florida to the southeast Newfoundland Ridge. *Deep-Sea Research Part I: Oceanographic Research Papers*, 112, 137–154.

- Michel, C., Terpstra, A. and Spengler, T. (2018) Polar mesoscale cyclone climatology for the Nordic Seas based on ERA-Interim. *Journal of Climate*, 31, 2511–2532.
- Milrad, S. (2017) *Synoptic Analysis and Forecasting: An Introductory Toolkit*. Elsevier, Amsterdam, Netherlands.
- Minobe, S., Kuwano-Yoshida, A., Komori, N., Xie, S.-P. and Small, R.J. (2008) Influence of the Gulf Stream on the troposphere. *Nature*, 452, 206–210.
- Murray, R.J. and Simmonds, I. (1991a) A numerical scheme for tracking cyclone centres from digital data. Part I: Development and operation of the scheme. *Australian Meteorological Magazine*, 39, 155–166.
- Murray, R.J. and Simmonds, I. (1991b) A numerical scheme for tracking cyclone centres from digital data. Part II: Application to January and July general circulation model simulations. *Australian Meteorological Magazine*, 39, 167–180.
- Nakamura, H., Sampe, T., Tanimoto, Y. and Shimpo, A. (2004) Observed associations among storm tracks, jet streams and midlatitude oceanic fronts. *Geophysical Monograph Series*, 147, 329–345.
- Neu, U., Akperov, M.G., Bellenbaum, N., Benestad, R., Blender, R., Caballero, R., Coccozza, A., Dacre, H.F., Feng, Y., Fraedrich, K., Grieger, J., Gulev, S., Hanley, J., Hewson, T., Inatsu, M., Keay, K., Kew, S.F., Kindem, I., Leckebusch, G.C., Liberato, M.L.R., Lionello, P., Mokhov, I.I., Pinto, J.G., Raible, C.C., Reale, M., Rudeva, I., Schuster, M., Simmonds, I., Sinclair, M., Sprenger, M., Tilinina, N.D., Trigo, I.F., Ulbrich, S., Ulbrich, U., Wang, X.L. and Wernli, H. (2013) IMILAST: A community effort to intercompare extratropical cyclone detection and tracking algorithms. *Bulletin of the American Meteorological Society*, 94, 529–547.
- Ogawa, F. and Spengler, T. (2019) Prevailing surface wind direction during air–sea heat exchange. *Journal of Climate*, 32, 5601–5617.
- Oruba, L., Lapeyre, G. and Rivière, G. (2013) On the poleward motion of midlatitude cyclones in a baroclinic meandering jet. *Journal of the Atmospheric Sciences*, 70, 2629–2649.
- Papritz, L. and Spengler, T. (2015) Analysis of the slope of isentropic surfaces and its tendencies over the North Atlantic. *Quarterly Journal of the Royal Meteorological Society*, 141, 3226–3238.
- Parfitt, R., Czaja, A., Minobe, S. and Kuwano-Yoshida, A. (2016) The atmospheric frontal response to SST perturbations in the Gulf Stream region. *Geophysical Research Letters*, 43, 2299–2306.
- Pfahl, S., O’Gorman, P.A. and Singh, M.S. (2015) Extratropical cyclones in idealized simulations of changed climates. *Journal of Climate*, 28, 9373–9392.
- Pfahl, S. and Sprenger, M. (2016) On the relationship between extratropical cyclone precipitation and intensity. *Geophysical Research Letters*, 43, 1752–1758.
- Reed, R.J., Grell, G.A. and Kuo, Y.-H. (1993) The ERICA IOP 5 storm. Part I: analysis and simulation. *Monthly Weather Review*, 121, 1577–1594.
- Renard, R.J. and Clarke, L.C. (1965) Experiments in numerical objective frontal analysis. *Monthly Weather Review*, 93, 547–556.
- Ritchie, E.A. and Elsberry, R.L. (2003) Simulations of the extratropical transition of tropical cyclones: Contributions by the midlatitude upper-level trough to reintensification. *Monthly Weather Review*, 131, 2112–2128.
- Riviere, G. and Joly, A. (2006) Role of the low-frequency deformation field on the explosive growth of extratropical cyclones at the jet exit. Part II: Baroclinic critical region. *Journal of the Atmospheric Sciences*, 63, 1982–1995.
- Roebber, P.J. (1989) The role of surface heat and moisture fluxes associated with large-scale ocean current meanders in maritime cyclogenesis. *Monthly Weather Review*, 117, 1676–1694.
- Rogers, E. and Bosart, L.F. (1991) A diagnostic study of two intense oceanic cyclones. *Monthly Weather Review*, 119, 965–996.
- Rudeva, I. and Gulev, S.K. (2011) Composite analysis of North Atlantic extratropical cyclones in NCEP–NCAR reanalysis data. *Monthly Weather Review*, 139, 1419–1446.
- Sanders, F. (1986) Explosive cyclogenesis in the west-central North Atlantic Ocean, 1981–84. Part I: Composite structure and mean behavior. *Monthly Weather Review*, 114, 1781–1794.
- Sanders, F. and Gyakum, J.R. (1980) Synoptic-dynamic climatology of the “bomb”. *Monthly Weather Review*, 108, 1589–1606.
- Schemm, S., Rudeva, I. and Simmonds, I. (2015) Extratropical fronts in the lower troposphere – global perspectives obtained from two automated methods. *Quarterly Journal of the Royal Meteorological Society*, 141, 1686–1698.
- Schultz, D.M., Keyser, D. and Bosart, L.F. (1998) The effect of large-scale flow on low-level frontal structure and evolution in midlatitude cyclones. *Monthly Weather Review*, 126, 1767–1791.
- Sinclair, M.R. and Revell, M.J. (2000) Classification and composite diagnosis of extratropical cyclogenesis events in the southwest Pacific. *Monthly Weather Review*, 128, 1089–1105.
- Spensberger, C., Spengler, T. and Li, C. (2017) Upper-tropospheric jet axis detection and application to the boreal winter 2013/14. *Monthly Weather Review*, 145, 2363–2374.
- Thompson, K., Loucks, R. and Trites, R. (1988) Sea surface temperature variability in the shelf-slope region of the Northwest Atlantic. *Atmosphere Ocean*, 26, 282–299.
- Tomczak, M. and Godfrey, J. (2003) *Regional Oceanography: An Introduction*. Elsevier Science, Oxford, UK.
- Uccellini, L.W. (1990) Processes contributing to the rapid development of extratropical cyclones, pp. 81–105 in *Extratropical Cyclones*. Springer, Berlin.
- Uccellini, L.W., Kocin, P.J., Petersen, R.A., Wash, C.H. and Brill, K.F. (1984) The Presidents’ Day cyclone of 18–19 February 1979: Synoptic overview and analysis of the subtropical jet streak influencing the pre-cyclogenetic period. *Monthly Weather Review*, 112, 31–55.
- Vannière, B., Czaja, A. and Dacre, H.F. (2017a) Contribution of the cold sector of extratropical cyclones to mean state features over the Gulf Stream in winter. *Quarterly Journal of the Royal Meteorological Society*, 143, 1990–2000.
- Vannière, B., Czaja, A., Dacre, H.F. and Woollings, T. (2017b) A “Cold Path” for the Gulf Stream–troposphere connection. *Journal of Climate*, 30, 1363–1379.
- Wang, C.-C. and Rogers, J.C. (2001) A composite study of explosive cyclogenesis in different sectors of the North Atlantic. Part I: Cyclone structure and evolution. *Monthly Weather Review*, 129, 1481–1499.
- Weijenberg, C. and Spengler, T. (2020) Diabatic heating as a pathway for cyclone clustering encompassing the extreme storm *Dagmar*. *Geophysical Research Letters*, 47(8). <https://doi.org/10.1029/2019GL085777>.
- Whitaker, J.S. and Davis, C.A. (1994) Cyclogenesis in a saturated environment. *Journal of the Atmospheric Sciences*, 51, 889–908.
- Zolina, O. and Gulev, S.K. (2003) Synoptic variability of ocean–atmosphere turbulent fluxes associated with atmospheric cyclones. *Journal of Climate*, 16, 2717–2734.

How to cite this article: Tsopouridis L, Spensberger C, Spengler T. Characteristics of cyclones following different pathways in the Gulf Stream region. *Q.J.R. Meteorol. Soc.* 2021;147:392–407. <https://doi.org/10.1002/qj.3924>

APPENDIX

Namelists used when running the cyclone detection and tracking algorithm

TABLE A1 Values of the parameters for the detection and tracking namelists used by the algorithm (Murray and Simmonds, 1991a; 1991b; Michel *et al.*, 2018)

Cyclone detection					
ni, nj	301	drmx1	0.7	fccmn	0.0
rproj	150	drmx2	0.3	cvarad	1.25
rdiff	2.0	itmx1, itmx2	10	nrrdir	18
rdifz	2.0	diflt1, diflt2	2.0	rdincr	0.25
iopmxc	1	cmnh, cmnc	0.0	sphtrg	.false.
istmxc	11	cmnc1	0.5	rdpgrd	5.0
nshell	12	cmnc2	1.3	npgdir	12
mscrn	2	dpmn	0.1	ftopeq	0.005
sdrmx	10	zsmx	1000	cmncw	2.0
Tracking					
irevmx	400	refdt	0.25	qmxnew	0.75
wsteer	0.6	wpten	0.3	qmxopn	0.75
fsteer	2.0	wmotn	1.0	qmxwek	0.5
asteer	0.5	rcprob	12.0	rpbell	0.5